Weierstraß-Institut
für Angewandte Analysis und Stochastik

Leibniz-Institut im Forschungsverbund Berlin e. V.

Preprint ISSN 2198-5855

Reconstruction of quasi-local numerical effective models from low-resolution measurements

Alfonso Caiazzo[1], Roland Maier[2], Daniel Peterseim[2]

submitted: February 25, 2019

[1] Weierstrass Institute
Mohrenstr. 39
10117 Berlin, Germany
E-Mail: alfonso.caiazzo@wias-berlin.de

[2] University of Augsburg
Universitätsstr. 14
86159 Augsburg, Germany
E-Mail: {roland.maier,daniel.peterseim}@math.uni-augsburg.de

No. 2577
Berlin 2019

2010 *Mathematics Subject Classification.* 65N21, 65N30, 74Q05.

Key words and phrases. Inverse problem, multiscale methods, numerical homogenization.

Edited by
Weierstraß-Institut für Angewandte Analysis und Stochastik (WIAS)
Leibniz-Institut im Forschungsverbund Berlin e. V.
Mohrenstraße 39
10117 Berlin
Germany

Fax: +49 30 20372-303
E-Mail: preprint@wias-berlin.de
World Wide Web: http://www.wias-berlin.de/

Reconstruction of quasi-local numerical effective models from low-resolution measurements

Alfonso Caiazzo, Roland Maier, Daniel Peterseim

Abstract

We consider the inverse problem of reconstructing an effective model for a prototypical diffusion process in strongly heterogeneous media based on low-resolution measurements. We rely on recent quasi-local numerical effective models that, in contrast to conventional homogenized models, are provably reliable beyond periodicity assumptions and scale separation. The goal of this work is to show that the identification of the matrix representation of these effective models is possible. Algorithmic aspects of the inversion procedure and its performance are illustrated in a series of numerical experiments.

1 Introduction

Recent medical imaging protocols based on Magnetic Resonance Imaging (MRI) play a key role in non-invasive modern diagnostics. As an example, in Magnetic Resonance Elastography (MRE), displacement fields acquired via phase-constrast MRI are used, in combination with a mechanical tissue model, to recover information about the elastic behavior of the tissue [32, 39, 21]. However, the resolution of data, which is practically limited by examination time and by the properties of the MRI scanner, only allows for the reconstruction of tissue models on an effective scale (e.g., order of millimeters), which is typically much coarser than the characteristic length scales of the microstructures (e.g., vasculature) of living tissue.

This difficulty calls for mathematical models that describe the effective behavior of physical processes on the scale of data resolution while also incorporating microscopic information. Such models are the key to bridge the discrepancy between microstructural quantities and the effective behavior in the desired reconstruction process and are typically referred to as homogenized (or effective) models. Classical homogenization methods are based on analytical homogenization theory and rely on strong assumptions such as (local) periodicity or a clear separation of scales which cannot always be assumed for general microstructures, especially in the presence of pathological changes. In these cases, certain numerical homogenization methods provide an alternative. State-of-the-art techniques such as Localized Orthogonal Decomposition (LOD) provide effective models that provably cope with arbitrary rough coefficients in a large class of model problems including diffusion problems [27, 18], elasticity [19, 2] and wave propagation [14, 1, 37, 41, 13, 26], without requiring periodicity or scale separation. These methods are therefore natural candidates for the reconstruction of effective models on the macroscopic scale of data resolution in the very general setting.

As far as linear elliptic problems are concerned, there are various other numerical homogenization approaches such as the Generalized Finite Element Methods (GFEM) [3], AL bases [16], Rough Polyharmonic Splines (RPS) [35], the Generalized Multiscale Finite Element Method (GMsFEM) [11], Gamblets [33], CEM-GMsFEM [6], and their variants with similar properties as LOD. All these methods are

DOI 10.20347/WIAS.PREPRINT.2577 Berlin 2019

based on a coarse mesh with a characteristic mesh parameter (typically the effective scale), or corresponding concepts in the setting of mesh-free methods, and compute special problem-adapted basis functions with optimal approximation properties. These methods are of Galerkin-type and thus characterized by discrete bases. To achieve optimal accuracy, a moderate price in terms of an overhead in the computational complexity has to be paid compared to a standard finite element method (fixed order) on the same mesh. The overhead is either in the number of functions per mesh entity (GFEM, GMsFEM), e.g., elements or nodes, or in the support of the basis functions (LOD, RPS, Gamblets, AL bases). In both cases, the result is an increased communication between the degrees of freedom which in turn leads to a slightly denser sparsity pattern of the corresponding system matrices. We will refer to these methods as quasi-local to differentiate from standard finite element methods that only have local communication between neighboring degrees of freedom. The quasi-locality also distinguishes the above numerical homogenization methods from classical numerical multiscale methods based on homogenization theory such as the Multiscale Finite Element Method (MsFEM) [22], the Two-Scale Finite Element Method [28], or the Heterogeneous Multiscale Method (HMM) [10, 9] that share the communication pattern of classical finite element methods.

We conclude that reliable effective models for PDEs with general microstructures are based on a controlled deviation from locality. Similar observations have been made in connection with the pollution effect in high-frequency time-harmonic wave propapation [4] which cannot be avoided unless the mesh size is coupled to, e.g., the polynomial degree [30, 31, 29] or the support of the basis functions [37] in a logarithmic way. Promising results using non-local models have also been achieved in the field of peridynamics [40, 25, 8]. All these findings motivate the use of quasi-local models in the context of inversion processes on the effective scale.

Although the quasi-local effective models described above are purely discrete and lack a PDE representation in general, they are well-understood. Hence, this paper follows the pragmatic approach of reconstructing quasi-local effective models (i.e., their matrix representation) given low-resolution measurements based on inhomogeneous boundary data in a medium with microstructures. The goal of this paper is to promote this idea along with some algorithmic aspects and numerical experiments that serve as a proof of concept. To demonstrate the feasibility and the potential of the approach, we consider a stationary linear elliptic multiscale diffusion model problem. For this PDE, we consider a worst-case scenario without any structural a priori knowledge on the underlying diffusion coefficient. In particular, we do not assume that the heterogeneous coefficient can be parameterized by a few unknown parameters that could easily be identified.

We start with introducing the microscopic forward problem and derive the effective model, represented by the effective stiffness matrix, by adapting existing theory from numerical homogenization (Section 2). This is mainly to emphasize that an effective model indeed exists in the setting of very general coefficients. In the actual inversion process, we tackle the reconstruction of an effective quasi-local model from given measurements. To this end, we prescribe the quasi-locality of the system matrices and rephrase the inverse problem as a non-linear least squares problem for which we discuss iterative minimization techniques such as the gradient descent or the Gauß-Newton method (Section 3). In a series of numerical experiments (Section 4), we show that quasi-local effective models can indeed be reconstructed. In particular, we consider the case where we are given measurements for all possible (coarse) boundary conditions, and also the setting where solutions are only known for a few boundary conditions. The aim of the experiments is to show that allowing the model to deviate from true locality, in the sense of classical effective PDE models, improves the inversion process and, thus, justifies the previous discussion.

2 Microscopic Forward Problem and Effective Approximation beyond Homogenization

2.1 Problem setting

We consider the prototypical second-order linear elliptic diffusion problem

$$\begin{aligned} -\operatorname{div} A\nabla u &= f \quad && \text{in } \Omega, \\ u &= u^0 && \text{on } \partial\Omega, \end{aligned} \tag{2.1}$$

where $\Omega \subset \mathbb{R}^d$, $d \in \{1,2,3\}$ is a polyhedral domain and the diffusion coefficient A encodes the microstructure of the medium. We do not make any structural assumptions on the coefficient such as periodicity or scale separation. Admissible coefficients are elements of the following set,

$$\mathcal{A} := \left\{ \begin{array}{l} A \in L^\infty(\Omega; \mathbb{R}^{d\times d}_{\mathrm{sym}}) \,:\, \exists\, 0 < \alpha \le \beta < \infty \,: \\ \forall \xi \in \mathbb{R}^d, \text{ a.a. } x \in \Omega \,:\, \alpha|\xi|^2 \le A(x)\xi\cdot\xi \le \beta|\xi|^2 \end{array} \right\},$$

which only requires minimal assumptions.

Since solutions to problem (2.1) do not necessarily exist in the classical sense, we are interested in the weak solution of (2.1) in the Sobolev space $V := H^1(\Omega)$ which is characterized by the following variational formulation. Given $A \in \mathcal{A}$, $u^0 \in X := H^{1/2}(\partial\Omega)$, and $f \in L^2(\Omega)$, we seek $u \in V$ such that

$$\begin{aligned} a(u,v) &= (f,v) \quad && \text{for all } v \in V^0 := H^1_0(\Omega), \\ \operatorname{tr} u &= u^0 && \text{on } \partial\Omega, \end{aligned} \tag{2.2}$$

where $a(w,v) := \int_\Omega A\nabla w\cdot\nabla v \,\mathrm{d}x$ and $(w,v) := (w,v)_{L^2(\Omega)}$ denotes the L^2 inner product. Note that instead of (2.1), we could as well consider a general second-order linear PDE in divergence form with additional lower-order terms. Such a generalization is straight-forward but is omitted for simplicity.

In practice, it is favorable to rewrite problem (2.2) as a problem with homogeneous Dirichlet boundary conditions in V^0. Let $E^b\colon X \to V$ be a linear extension operator, which also defines the restriction operator $R\colon V \to V^0$ by $R := 1 - E^b \operatorname{tr}$. Then, we can decompose $u = Ru + (1-R)u = Ru + E^b u^0$ and problem (2.2) reduces to finding $Ru \in V^0$ such that

$$a(Ru, v) = (f,v) - a(E^b u^0, v) \tag{2.3}$$

for all $v \in V^0$.

2.2 Effective model via Localized Orthogonal Decomposition

Let us now introduce a *coarse* target scale H (e.g., the resolution of the data available for the inverse problem). We adopt the notation from numerical homogenization where a capital H is used to indicate that the scale is indeed a coarse one. In typical applications H will be much larger than the *microscopic* scale, i.e., the scale at which the diffusion coefficient varies. To represent the solution on the scale H, we discretize (2.3) by using the multiscale technique introduced in [27] known as Localized Orthogonal Decomposition (LOD).

Let $\mathcal{T}_H$ be a mesh of orthotopes with characteristic mesh size H and denote as $Q^1(\mathcal{T}_H)$ the corresponding space of piecewise bilinear functions. In order to introduce the LOD, we define the discrete

spaces $V_H := Q^1(\mathcal{T}_H) \cap V$, $V_H^0 := V_H \cap V^0$, and $X_H := \operatorname{tr} V_H$ with dimensions $m = \dim V_H$, $m^0 = \dim V_H^0$, and $n = \dim X_H$, respectively. The choice of these finite element spaces is not unique and other standard finite element spaces could be used. Since the standard space V_H is not suitable for the approximation of u if H is larger than the spatial scale of the microstructure, we enrich the coarse model with microscopic information about the problem via corrections of classical finite element functions. The construction of these corrections is based on a projective quasi-interpolation operator $I_H \colon V^0 \to V_H^0$ with standard approximation and stability properties, i.e., for an element $T \in \mathcal{T}_H$ with diameter H_T, it holds that

$$\|H_T^{-1}(v - I_H v)\|_{L^2(T)} + \|\nabla I_H v\|_{L^2(T)} \leq C\|\nabla v\|_{L^2(\mathrm{N}(T))} \tag{2.4}$$

for all $v \in V^0$, where the constant C is independent of H, and

$$\mathrm{N}(\omega) := \bigcup \{T \in \mathcal{T}_H \,:\, \overline{T} \cap \overline{\omega} \neq \emptyset\}$$

defines the neighborhood of $\omega \subset \Omega$. Note that for shape-regular meshes the above estimate also holds globally. For a particular choice of I_H, see [12, 15, 24].

Based on I_H, we define, for any element $T \in \mathcal{T}_H$ and any function $v_H \in V_H^0$, the element correction $\mathcal{C}_T v_H \in W := \operatorname{Ker} I_H$ by

$$a(\mathcal{C}_T v_H, w) = \int_T A\nabla v_H \cdot \nabla w =: a_T(v_H, w) \tag{2.5}$$

for all $w \in W$, and the full correction $\mathcal{C} \colon V_H^0 \to W$ by

$$\mathcal{C} := \sum_{T \in \mathcal{T}_H} \mathcal{C}_T.$$

By construction, it holds that

$$a((1 - \mathcal{C})v_H, w) = 0 \tag{2.6}$$

for all $v_H \in V_H^0$ and $w \in W$. The corrections $\mathcal{C}_T v_H$ have, in general, global support. However, as shown in [20, 36] (based on [27]) they decay exponentially fast (see also the one-dimensional sketch in Figure 2.1). Therefore, we use localized element corrections $\mathcal{C}_{T,\ell} v_H$ which are obtained by solving (2.5) on local patches with ℓ layers, i.e.,

$$a(\mathcal{C}_{T,\ell} v_H, w) = a_T(v_H, w) \tag{2.7}$$

for all $w \in W$ with $w|_{\Omega \setminus \mathrm{N}^\ell(T)} = 0$. The ℓ-neighborhood N^ℓ is defined as

$$\mathrm{N}^\ell(\omega) = \mathrm{N}(\mathrm{N}^{\ell-1}(\omega)),\ \ell \geq 1, \qquad \mathrm{N}^0(\omega) := \bigcup \{T \in \mathcal{T}_H \,:\, \omega \subset \overline{T}\}$$

for $\omega \subset \Omega$. As above, we define the full correction $\mathcal{C}_\ell \colon V_H^0 \to W$ by

$$\mathcal{C}_\ell := \sum_{T \in \mathcal{T}_H} \mathcal{C}_{T,\ell}.$$

As shown in [20], we get, for any $v_H \in V_H^0$,

$$\|\nabla(\mathcal{C} - \mathcal{C}_\ell)v_H\|_{L^2(\Omega)} \leq e^{-c\ell}\|\nabla v_H\|_{L^2(\Omega)}. \tag{2.8}$$

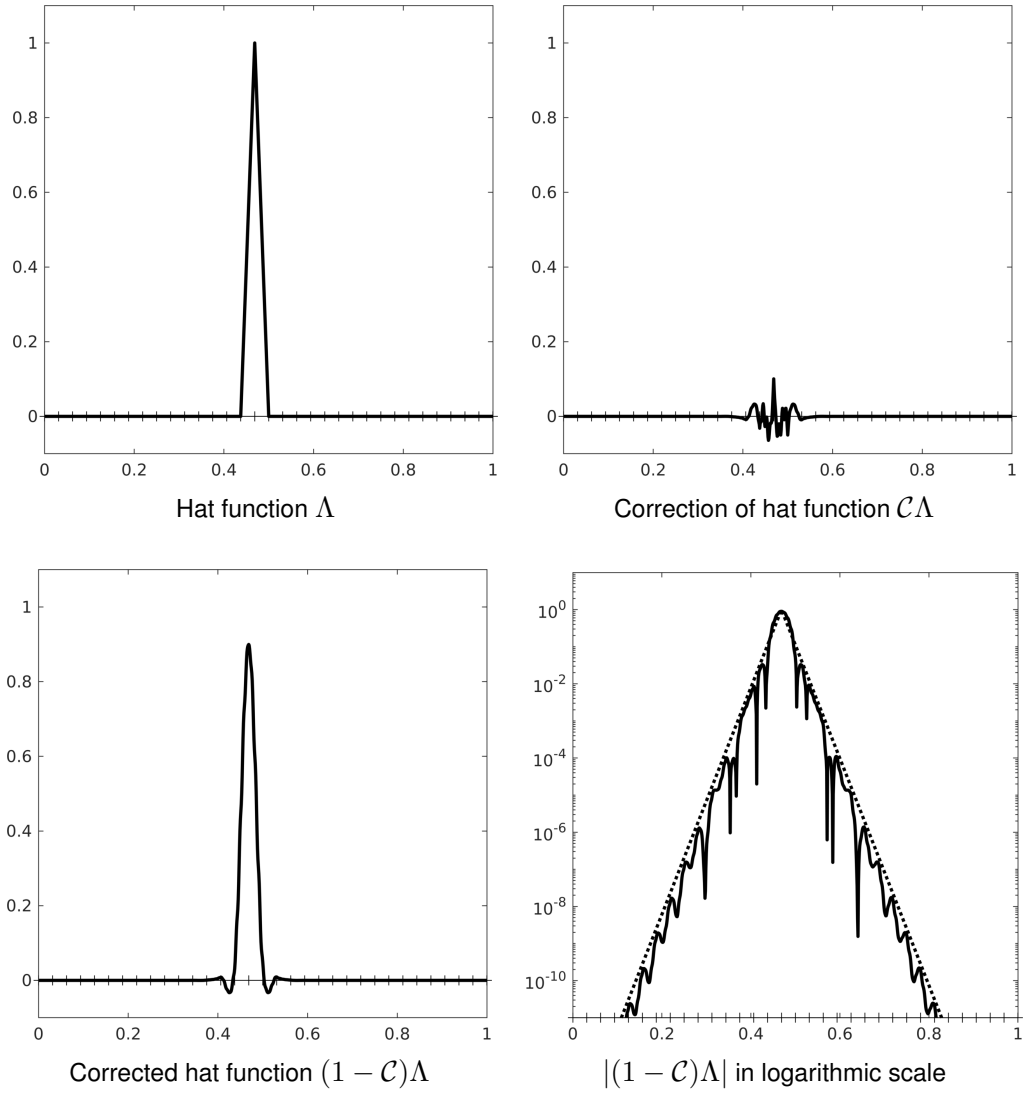

Figure 2.1: Illustration of a one-dimensional hat function and its correction for the coefficient $A(x) = (2 + \sin(2^8\pi x))^{-1}$.

The constant c only depends on the contrast β/α, although this dependence seems pessimistic in many cases of practical relevance [38, 17]. For $v_H \in V_H$, we set $\mathcal{C}v_H := \mathcal{C}Rv_H$ and $\mathcal{C}_\ell v_H := \mathcal{C}_\ell R v_H$.

Given a discretized extension operator $E_H^b \colon X_H \to V_H$ that fulfills $E^b|_{X_H} = E_H^b$ and the corresponding restriction operator $R_H \colon V_H \to V_H^0$ defined by $R_H := 1 - E_H^b \operatorname{tr}$, the discretized version of (2.3) reads: find $u_H = R_H u_H + E_H^b u_H^0 \in V_H$ such that

$$a((1-\mathcal{C}_\ell)R_H u_H, (1-\mathcal{C}_\ell)v_H) = (f_H, v_H) - a(E_H^b u_H^0, (1-\mathcal{C}_\ell)v_H) \tag{2.9}$$

for all $v_H \in V_H^0$. In (2.9), $f_H := \Pi_H f$ is the L^2 projection of f onto V_H, and u_H^0 a finite element approximation of u^0. In the context of inverse problems, it is reasonable to consider that u^0 is defined as the first order finite element approximation of coarse experimental boundary data which approximate the real data up to order H in the $H^{1/2}$ norm. Thus, in the following we will assume that $u^0 = u_H^0$.

2.3 Error estimates

The following theorem shows that the approximation error of the presented approach scales optimally with H and that it is independent of the variations of the diffusion coefficient.

Theorem 2.1 (Error of the forward effective model) *Let $u \in V$ be the solution of* (2.2) *and $u_H \in V_H$ the solution of* (2.9)*, for given boundary data $u^0 \in X_H$, a right-hand side $f \in L^2(\Omega)$, as well as an oversampling parameter ℓ.*

For $g \in L^2(\Omega)$, let $\hat{u}(g) \in V$ denote the solution of (2.2) *with right-hand side g and boundary condition $u^0 = 0$, and let us introduce the worst-case best-approximation error*

$$\mathbf{wcba}(A, \mathcal{T}_H) := \sup_{g \in L^2(\Omega)\setminus\{0\}} \inf_{v_H \in V_H^0} \frac{\|R\hat{u}(g) - v_H\|_{L^2(\Omega)}}{\|g\|_{L^2(\Omega)}}.$$

It holds

$$\|u - u_H\|_{L^2(\Omega)} \lesssim \left(H^2 + e^{-c\ell} + \mathbf{wcba}(A, \mathcal{T}_H)\right)\left(\|f\|_{L^2(\Omega)} + \|u^0\|_X\right).$$

Proof of Theorem 2.1. We split the error $u - u_H = (u - \bar{u}_H) + (\bar{u}_H - \tilde{u}_H) + (\tilde{u}_H - u_H)$ with the solutions $\bar{u}_H$ and $\tilde{u}_H$ of the auxiliary problems

$$a(R_H \bar{u}_H, (1-\mathcal{C})v_H) = (f, v_H) - a(E_H^b u^0, (1-\mathcal{C})v_H)$$

and

$$a(R_H \tilde{u}_H, (1-\mathcal{C}_\ell)v_H) = (f_H, v_H) - a(E_H^b u^0, (1-\mathcal{C}_\ell)v_H).$$

To bound $e_H := u_H - \tilde{u}_H$, we observe that

$$a((1-\mathcal{C}_\ell)e_H, (1-\mathcal{C}_\ell)v_H) = -a(\mathcal{C}_\ell R_H \tilde{u}_H, (1-\mathcal{C}_\ell)v_H) = a(\mathcal{C}_\ell R_H \tilde{u}_H, (\mathcal{C}_\ell - \mathcal{C})v_H), \tag{2.10}$$

by the orthogonality property (2.5). Testing with $v_H = e_H$ in (2.10) and using (2.8), it follows that

$$\begin{aligned}
\|A^{1/2}\nabla(1-\mathcal{C}_\ell)e_H\|_{L^2(\Omega)}^2 &= a((1-\mathcal{C}_\ell)e_H, (1-\mathcal{C}_\ell)e_H) \\
&= a(\mathcal{C}_\ell R_H \tilde{u}_H, (\mathcal{C}_\ell - \mathcal{C})e_H) \\
&\lesssim e^{-c\ell}\|\nabla \mathcal{C}_\ell R_H \tilde{u}_H\|_{L^2(\Omega)}\|A^{1/2}\nabla(1-\mathcal{C}_\ell)e_H\|_{L^2(\Omega)}^2
\end{aligned}$$

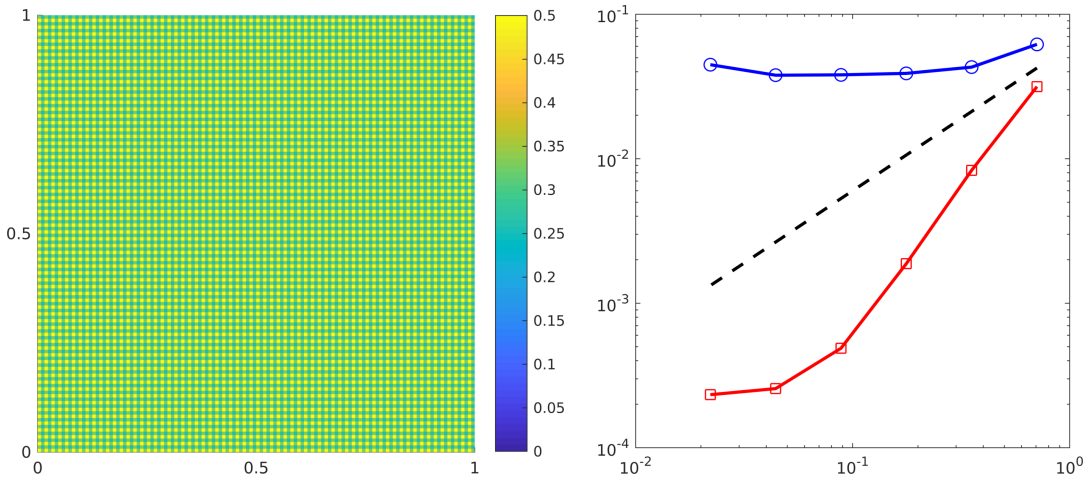

Coefficient A L^2 errors of FEM (○) and LOD (□)

Figure 2.2: Left: An example of a fine scale coefficient. Right: Comparison of the finite element method and the LOD on $\Omega = [0,1]^2$ for $f = 1$, $u^0 = 0$, and $\ell = 2$ for the solution of the diffusion problem corresponding to the depicted scalar coefficient. The dashed line indicates linear convergence.

and thus

$$\|e_H\|_{L^2(\Omega)} \lesssim \|A^{1/2}\nabla(1-\mathcal{C}_\ell)e_H\|_{L^2(\Omega)} \lesssim e^{-c\ell}\left(\|f\|_{L^2(\Omega)} + \|u^0\|_X\right) \tag{2.11}$$

using $e_H = I_H(1-\mathcal{C}_\ell)e_H$ and (2.4). As a next step, we bound $\bar{e}_H := \tilde{u}_H - \bar{u}_H$. We note that

$$a(\bar{e}_H, (1-\mathcal{C})v_H) = a(R_H\tilde{u}_H + E_H^b u^0, (\mathcal{C}-\mathcal{C}_\ell)v_H)$$

for any $v_H \in V_H^0$. With $v_H = \bar{e}_H$ and similar arguments as above, we obtain

$$\|\bar{e}_H\|_{L^2(\Omega)} \lesssim \|A^{1/2}\nabla(1-\mathcal{C})\bar{e}_H\|_{L^2(\Omega)} \lesssim e^{-c\ell}\left(\|f\|_{L^2(\Omega)} + \|u^0\|_X\right). \tag{2.12}$$

The error $u - \bar{u}_H$ can be estimated using [15, Proposition 1] which also holds for inhomogeneous Dirichlet boundary conditions, i.e.,

$$\|u - \bar{u}_H\|_{L^2(\Omega)} \lesssim \left(H^2 + \mathbf{wcba}(A, \mathcal{T}_H)\right)\left(\|f\|_{L^2(\Omega)} + \|u^0\|_X\right). \tag{2.13}$$

The triangle inequality, (2.11), (2.12), and (2.13) yield the desired estimate. To illustrate the advantage of the LOD, Figure 2.2 shows the error between the numerical solution on a fine scale and the numerical solutions using the LOD and a classical finite element approximation on a coarse scale, respectively. The finite element method suffers from pre-asymptotic effects when the micro scale is not resolved, while the LOD produces a finite element function with much better approximation properties.

We emphasize that, choosing ℓ large enough (i.e., $\ell \gtrsim |\log H|$), it holds $e^{-c\ell} \lesssim H$ or even $e^{-c\ell} \lesssim H^2$. As discussed in [15], the worst-case best-approximation error is at least $\mathcal{O}(H)$, and it scales possibly even better with H for certain pre-asymptotic regimes. In this work, we are mainly interested in solving the inverse problem and do not focus on optimizing the error estimates derived above.

To prepare the setting for the inverse problem, we define the solution operator

$$\begin{aligned} \mathfrak{L}_A \colon X_H \times L^2(\Omega) &\to V, \\ (u^0, f) &\mapsto u, \text{ where } u \text{ solves (2.2)} \end{aligned} \tag{2.14}$$

and its discretized version

$$\begin{aligned} \mathfrak{L}^{\mathrm{eff}}_{A,\ell}\colon X_H \times L^2(\Omega) &\to V_H, \\ (u^0, f) &\mapsto u_H, \text{ where } u_H \text{ solves (2.9).} \end{aligned} \tag{2.15}$$

The operator $\mathfrak{L}_A$ (and similarly also $\mathfrak{L}^{\mathrm{eff}}_{A,\ell}$) can be written as

$$\mathfrak{L}_A(u^0, f) = \mathfrak{L}_A(u^0, 0) + \mathfrak{L}_A(0, f) \tag{2.16}$$

with the linear operators $\mathfrak{L}_A(\cdot, 0)\colon X_H \to V$ and $\mathfrak{L}_A(0, \cdot)\colon L^2(\Omega) \to V$. For simplicity, we assume in the following that f is a fixed function. The generalization to the case where f is also part of the input data is conceptually straightforward but slightly more involved. The decomposition (2.16) motivates the distance function between operators defined by

$$\mathtt{dist}_f(\mathfrak{A}, \mathfrak{B}) := \left(\|\mathfrak{A}(\cdot, 0) - \mathfrak{B}(\cdot, 0)\|^2_{\mathcal{L}(X_H;V)} + \|\mathfrak{A}(0, f) - \mathfrak{B}(0, f)\|^2_V\right)^{1/2} \tag{2.17}$$

for all $\mathfrak{A}$, $\mathfrak{B}\colon X_H \times L^2(\Omega) \to V$.

Remark 2.2 *If we consider the case where $f = 0$, coefficients that only differ by a multiplicative constant produce the same solution operator. In view of the inverse problem in the next section, one should fix an additional parameter in this case, e.g., the mean value of A.*

Using Theorem 2.1, we obtain the following result.

Corollary 2.3 (Error of the effective forward operator) *Let $\ell \gtrsim |\log H|$. It holds that*

$$\mathtt{dist}_f(\mathfrak{L}_A, \mathfrak{L}^{\mathrm{eff}}_{A,\ell}) \lesssim H.$$

2.4 Reformulation of the effective model in terms of the effective stiffness matrix

As a next step, we discuss an alternative representation of the operator $\mathfrak{L}^{\mathrm{eff}}_{A,\ell}$ using the stiffness matrix corresponding to the discrete formulation (2.9). Given a coefficient $A \in \mathcal{A}$, the corresponding LOD stiffness matrix $S_H(A, \ell)$ is defined by

$$S_H(A, \ell)[i, j] := a((1 - \mathcal{C}_\ell)\Lambda_{z_j}, (1 - \mathcal{C}_\ell)\Lambda_{z_i}), \text{ for } i, j \in \{1, \dots, m\}, \tag{2.18}$$

where $i \mapsto z_i$ is a fixed ordering of the m nodes in $\mathcal{T}_H$ and Λ_z denotes the classical finite element hat function associated with the node $z \in \mathcal{T}_H$. The typical sparsity of such a matrix is depicted in Figure 2.3.

The set of LOD stiffness matrices with oversampling parameter ℓ based on admissible coefficients is given by

$$\mathcal{S}(\ell, \mathcal{T}_H) := \left\{S_H(A, \ell) \in \mathbb{R}^{m\times m}_{\mathrm{sym}} \,:\, A \in \mathcal{A}\right\}. \tag{2.19}$$

For any matrix $S_H \in \mathcal{S}(\ell, \mathcal{T}_H)$, we define the operator

$$\begin{aligned} \mathfrak{L}^{\mathrm{eff}}_{S_H}\colon X_H \times L^2(\Omega) &\to V_H, \\ (u^0, f) &\mapsto u_H, \text{ where } u_H \text{ solves} \\ &\qquad \begin{cases} S_{H,0} R_H u_H = R_H M_H f_H - R_H S_H E^b_H u^0, \\ u_H = u^0 \text{ on } \partial\Omega, \end{cases} \end{aligned} \tag{2.20}$$

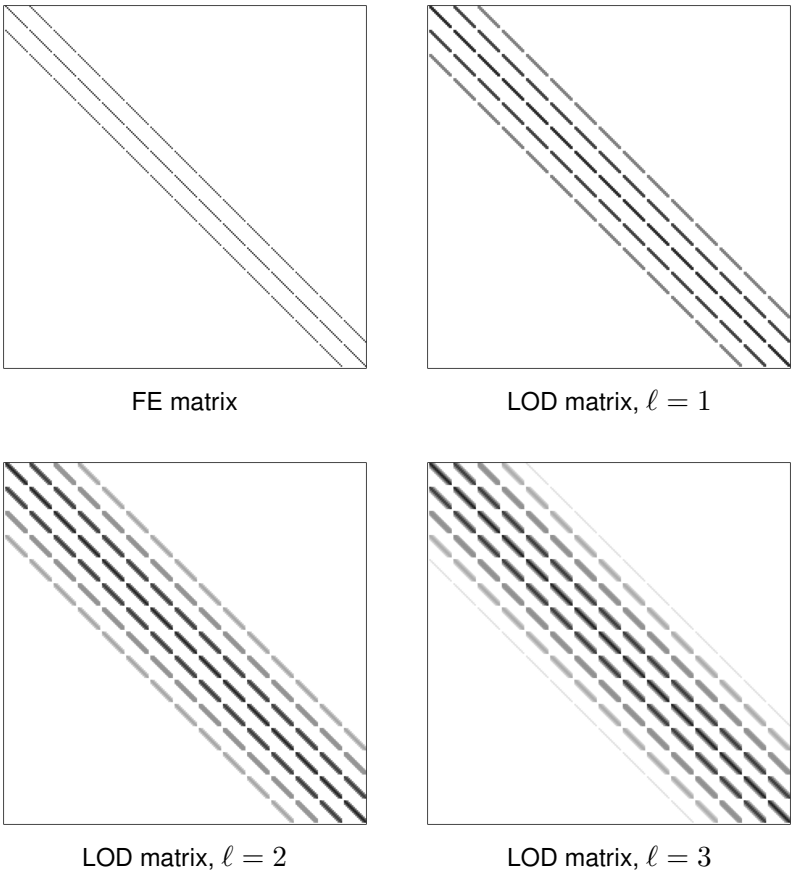

Figure 2.3: Sparsity pattern of a classical finite element stiffness matrix and LOD stiffness matrices for different values of ℓ on a Cartesian grid with lexicographic ordering in two dimensions.

with the classical finite element mass matrix M_H and the restriction $S_{H,0} = R_H S_H {R_H}^T$ of S_H to the inner nodes of $\mathcal{T}_H$. Recall that $f_H = \Pi_H f$. For better readability, we use the notation v_H (or B_H) for both the vector $v_H \in \mathbb{R}^m$ (or the matrix $B_H \in \mathbb{R}^{m^0 \times m}$) and the corresponding function $v_H \in V_H$ (or the mapping $B_H \colon V_H \to V_H^0$). In this setting, we can prove the following lemma.

Lemma 2.4 (Alternative representation of the effective forward operator) *Let $S_H(A,\ell) \in \mathcal{S}(\ell, \mathcal{T}_H)$ be the LOD stiffness matrix corresponding to* (2.9)*. Assume that E^b fulfills $\mathcal{C}_\ell E_H^b v^0 = \mathcal{C}_\ell E^b|_{X_H} v^0 = 0$ for any $v^0 \in X_H$. It holds*

$$\mathfrak{L}^{\mathrm{eff}}_{S_H(A,\ell)}(u^0, f) = \mathfrak{L}^{\mathrm{eff}}_{A,\ell}(u^0, f) \tag{2.21}$$

for all $u^0 \in X_H,\ f \in L^2(\Omega)$.

Remark 2.5 *Possible choices for the extension operator E^b that fulfill the assumptions of Lemma 2.4 are those that extend functions in X_H to functions in V_H that are only supported on one layer of elements away from the boundary.*

Proof of Lemma 2.4. Write $u_H = \sum_{j=1}^m u_j \Lambda_{z_j}$ and observe that (2.9) is equivalent to

$$\sum_{j\,:\,z_j \notin \partial\Omega} u_j\, a((1-\mathcal{C}_\ell) R_H \Lambda_{z_j}, (1-\mathcal{C}_\ell)\Lambda_{z_i}) = (f_H, \Lambda_{z_i}) - a(E_H^b u^0, (1-\mathcal{C}_\ell)\Lambda_{z_i}) \tag{2.22}$$

for all $i \in \{k \,:\, z_k \notin \partial\Omega\}$. Inserting $f_H = \sum_{j=1}^m f_j \Lambda_{z_i}$, using the fact that

$$a(E_H^b u_H^0, (1-\mathcal{C}_\ell) v_H) = a((1-\mathcal{C}_\ell) E_H^b u_H^0, (1-\mathcal{C}_\ell) v_H)$$

for any $v_H \in V_H^0$, and the definition (2.18), equation (2.22) can be written as

$$S_{H,0}(A,\ell) R_H u_H = R_H M_H f_H - R_H S_H(A,\ell) E_H^b u^0,$$

which shows (2.21). Lemma 2.4 and Theorem 2.3 show that the operators $\mathfrak{L}_A(\cdot, f)$ and $\mathfrak{L}^{\mathrm{eff}}_{S_H(A,\ell)}(\cdot, f)$ are close as operators from X_H to V if ℓ is chosen large enough. We will use this property in the next section to motivate the inverse problem.

3 Inverse Problem: Reconstruction of the Effective Model

3.1 Problem setting

Let us assume that the diffusion coefficient A is unknown and that structural assumptions such as periodicity, quasi-periodicity, and given parameterization by few degrees of freedom are not satisfied a priori. In an ideal setting, information about solutions to problem (2.2) in the form of a solution operator

$$\tilde{\mathfrak{L}} := \mathfrak{L}_A(\cdot, f) \colon X \to V$$

would be given. In practical applications, however, boundary data and information about the corresponding solutions are only available on some (coarse) scale, possibly much larger than the (micro) scale on which the diffusion coefficient and the corresponding solutions vary. In this case, a classical formulation of the inverse problem, for a fixed right-hand side f, consists in recovering A in (2.2) given the mapping

$$\tilde{\mathfrak{L}}^{\mathrm{eff}} := \mathfrak{L}^{\mathrm{eff}}_A(\cdot, f) \colon X_H \to V_H$$

which comprises coarse measurements of solutions to (2.2).

If the unknown coefficient includes fine scale features, a direct approach of recovering A by full (fine scale) simulations is computationally unfeasible. Inspired by the ideas presented in Section 2, we present in this section an alternative approach to recover information about the (macroscopic) effective model taking into account the presence of a micro scale diffusion coefficient. Rather than reconstructing the diffusion coefficient itself, we tackle the reconstruction of an effective stiffness matrix that is able to reproduce the given data related to solutions to (2.2). We recall that such an approach is reasonable since the mapping $\tilde{\mathfrak{L}}^{\mathrm{eff}}$ can not only be characterized by the corresponding coefficient but also by the effective stiffness matrix. Therefore, the alternative formulation of the inverse problem reads:

$$\text{given } \tilde{\mathfrak{L}}^{\mathrm{eff}}\colon X_H \to V_H, \text{ find the corresponding stiffness matrix } \tilde{S}_H.$$

Remark 3.1 *The process of finding a (sparse) matrix $\tilde{S}_H$ that is able to describe the behavior of a (dense) solution operator $\tilde{\mathfrak{L}}^{\mathrm{eff}}$ could also be seen as a technique for data compression.*

Remark 3.2 *Note that in the case $f = 0$, the classical Calderon problem [5] might be considered, where a so-called* Dirichlet-to-Neumann mapping *is given, instead of the operator $\mathfrak{L}_A$. However, this problem requires information on the coefficient at the boundary, and the derivation of the method presented below needs to be adjusted accordingly.*

3.2 The minimization problem

Ideally, the inverse problem would be formulated as a minimization problem for the functional

$$\tilde{\mathcal{J}}_H(S_H) = \frac{1}{2}\Big(\mathtt{dist}_f(\tilde{\mathfrak{L}}^{\mathrm{eff}}, \mathfrak{L}^{\mathrm{eff}}_{S_H})\Big)^2 \tag{3.1}$$

in the set $\mathcal{S}(\ell, \mathcal{T}_H)$ of LOD stiffness matrices based on admissible coefficients.

Since we are not able to characterize the set $\mathcal{S}(\ell, \mathcal{T}_H)$ in a way that would be suitable for optimization, we instead seek a minimizer in the linear space

$$\mathcal{M}(\ell, \mathcal{T}_H) := \big\{S_H \in \mathbb{R}^{m\times m}_{\mathrm{sym}} \,:\, \forall\, 0 \le i \le j \le m \,:\, z_i \notin \mathrm{N}^\ell(z_j) \Rightarrow S_H[i,j] = 0\big\} \tag{3.2}$$

of matrices that have a non-zero entry at position $[i, j]$ if the corresponding nodes z_i and z_j belong to the ℓ-neighborhood of each other. In other words, we enlarge the set of possible minimizers to all the matrices with a sparsity pattern that mimics the sparsity of LOD stiffness matrices (see also Figure 2.3). We emphasize that at this point the sole criterion in the inversion process is the sparsity pattern. From now on, we are searching for effective models with increased communication between the degrees of freedom without requiring any knowledge on LOD or other numerical homogenization methods.

Remark 3.3 *Observe that, by construction of the correctors $\mathcal{C}_\ell$ in* (2.7)*, it holds $\mathcal{S}(\ell, \mathcal{T}_H) \subset \mathcal{M}(\ell, \mathcal{T}_H)$. Note as well that stiffness and mass matrices arising from classical finite element methods belong to the space $\mathcal{M}(0, \mathcal{T}_H)$. Classical homogenization approaches such as the MsFEM without oversampling, the Two-Scale Finite Element Method, or the HMM also lead to stiffness matrices in $\mathcal{M}(0, \mathcal{T}_H)$. Matrices arising from the MsFEM with oversampling are included in $\mathcal{M}(1, \mathcal{T}_H)$.*

Remark 3.4 *It is worth noting that the set of matrices with the considered sparsity pattern includes matrices that occur in isogeometric analysis [23, 7]. Moreover, the set $\mathcal{M}(\ell, \mathcal{T}_H)$ also includes higher-order finite element matrices with polynomial degree $p \approx \ell$ on meshes that are coarser by roughly a factor of p and matrices from peridynamics with horizon $\delta \approx H\ell$.*

The minimization problem in $\mathcal{M}(\ell, \mathcal{T}_H)$ reads

$$\text{find } \tilde{S}_H^* = \arg \min_{S_H \in \mathcal{M}(\ell, \mathcal{T}_H)} \tilde{\mathcal{J}}_H(S_H). \tag{3.3}$$

Using the previously introduced matrices, the operator $\mathfrak{L}_{S_H}^{\text{eff}} \colon X_H \to V_H$ can be written as a matrix of size $m \times n$, i.e.,

$$\mathfrak{L}_{S_H}^{\text{eff}} = \mathfrak{L}_{S_H}^{\text{eff}}(\cdot, f) = \left(\mathbb{1} - {R_H}^T S_{H,0}^{-1} R_H S_H\right) E_H^b + {R_H}^T S_{H,0}^{-1} R_H M_H F_H,$$

with $F_H := [f_H, f_H, \dots, f_H] \in \mathbb{R}^{m \times n}$ and the identity matrix $\mathbb{1} \in \mathbb{R}^{m \times m}$. The operator $\tilde{\mathfrak{L}}^{\text{eff}}$ may also be interpreted as a matrix, so that the distance between the operators can be measured in general matrix norms. This is especially useful since a splitting of the form (2.16) is generally not known for $\tilde{\mathfrak{L}}^{\text{eff}}$.

Let $\mu := \dim \mathcal{M}(\ell, \mathcal{T}_H)$. Instead of (3.3), based on the matrix representation introduced above we consider a minimization problem for the functional $\mathcal{J}_H \colon \mathbb{R}^\mu \to \mathbb{R}$ defined by

$$\mathcal{J}_H(S_H) = \frac{1}{2} \left\| \tilde{\mathfrak{L}}^{\text{eff}} \right\|_{\mathbb{R}^{m \times n}}^{-2} \left\| \tilde{\mathfrak{L}}^{\text{eff}} - \mathfrak{L}_{S_H}^{\text{eff}} \right\|_{\mathbb{R}^{m \times n}}^2. \tag{3.4}$$

At this stage, the choice of the norm in $\mathbb{R}^{m \times n}$ in (3.4) is arbitrary. The results that we will show in Section 4 have been obtained using the Frobenius norm, which seems to be a natural candidate.

3.3 Iterative minimization

In order to find a minimizer of (3.4), we can now apply standard minimization techniques such as the *Newton method* or the *gradient descent method*. Here, we adopt a Gauß-Newton method which, in our numerical computations, showed faster convergence in terms of number of iterations.

In order to compute the descent direction, the most important step concerns the computation of the gradient of $\mathcal{J}_H$ with respect to the *relevant entries* $\{s_i\}_{i=1}^\mu$ of S_H (i.e., the diagonal and the non-zero entries above the diagonal, due to symmetry). Using the chain rule, we obtain

$$\frac{\partial}{\partial s_i} \mathcal{J}_H(S_H) = -\left\| \tilde{\mathfrak{L}}^{\text{eff}} \right\|_{\mathbb{R}^{m \times n}}^{-2} \left(\tilde{\mathfrak{L}}^{\text{eff}} - \mathfrak{L}_{S_H}^{\text{eff}} \right) : \frac{\partial \mathfrak{L}_{S_H}^{\text{eff}}}{\partial s_i}, \tag{3.5}$$

For the Gauß-Newton method, only the derivatives of $\mathfrak{L}_{S_H}^{\text{eff}}$ are needed, i.e.,

$$\begin{aligned} \frac{\partial \mathfrak{L}_{S_H}^{\text{eff}}}{\partial s_i} &= -{R_H}^T \left(\frac{\partial S_{H,0}^{-1}}{\partial s_i} \right) R_H (S_H E_H^b - M_H F_H) - {R_H}^T S_{H,0}^{-1} R_H \left(\frac{\partial S_H}{\partial s_i} \right) E_H^b \\ &= {R_H}^T S_{H,0}^{-1} \left(\frac{\partial S_{H,0}}{\partial s_i} \right) S_{H,0}^{-1} R_H (S_H E_H^b - M_H F_H) - {R_H}^T S_{H,0}^{-1} R_H \left(\frac{\partial S_H}{\partial s_i} \right) E_H^b. \end{aligned}$$

Here, the double dot product is defined by $M : \tilde{M} = \operatorname{trace}(M\tilde{M})$. The derivatives $\frac{\partial S_H}{\partial s_i}$ and $\frac{\partial S_{H,0}}{\partial s_i}$ are relatively easy to compute, as they are defined as global matrices that only contain at most two entries equal to 1.

For ease of notation, let us interpret $\mathfrak{L}^{\mathrm{eff}}_{S_H}$ and S_H as vectors in $\mathbb{R}^{mn}$ and $\mathbb{R}^{m^2}$, respectively. The Gauß-Newton method to minimize the functional $\mathcal{J}_H$ is then defined by the following steps.

- Let an initial matrix $S_H^0 \in \mathcal{M}(\ell, \mathcal{T}_H)$ be given.
- For $k = 0, 1, \ldots$ (until a certain stopping criterion is satisfied), solve

$$H_k p_k = \left[D\mathfrak{L}^{\mathrm{eff}}_{S_H^k} \right]^T \left[\tilde{\mathfrak{L}}^{\mathrm{eff}} - \mathfrak{L}^{\mathrm{eff}}_{S_H^k} \right] \tag{3.6}$$

  where D denotes the derivative with respect to the relevant entries of S_H and

$$H_k = \left[D\mathfrak{L}^{\mathrm{eff}}_{S_H^k} \right]^T \left[D\mathfrak{L}^{\mathrm{eff}}_{S_H^k} \right].$$

- Set $P_k \in \mathcal{M}(\ell, \mathcal{T}_H)$ as the matrix whose relevant entries are given by p_k and define

$$S_H^{k+1} = S_H^k + \delta_k P_k \tag{3.7}$$

  with appropriately chosen *step size* δ_k, for example using *backtracking line search* based on the *Armijo-Goldstein condition*.

Due to the ill-posedness of the inverse problem, the matrix H_k might be singular. A possible approach to overcome this issue consists in replacing (3.6) with

$$\left(H_k + \eta \mathbb{1}\right) p_k = \left[D\mathfrak{L}^{\mathrm{eff}}_{S_H^k} \right]^T \left[\tilde{\mathfrak{L}}^{\mathrm{eff}} - \mathfrak{L}^{\mathrm{eff}}_{S_H^k} \right] \tag{3.8}$$

with a given parameter $\eta > 0$.

Another possible strategy consists in adding a regularization term to the functional to be minimized, i.e., in replacing (3.4) by

$$\mathcal{J}_H(S_H) = \frac{1}{2} \left\| \tilde{\mathfrak{L}}^{\mathrm{eff}} \right\|^{-2}_{\mathbb{R}^{m\times n}} \left\| \tilde{\mathfrak{L}}^{\mathrm{eff}} - \mathfrak{L}^{\mathrm{eff}}_{S_H} \right\|^2_{\mathbb{R}^{m\times n}} + \frac{\gamma}{2} \left\| S_{\mathrm{reg}} - S_H \right\|^2_{R^{m\times m}} \tag{3.9}$$

where $\gamma > 0$ is a given regularization parameter and S_{reg} is a regularization (or stabilization) matrix. Additionally, the computations of the gradient in (3.5) need to be adapted accordingly. In the presence of multiple minimizers, this regularization enforces the solution to be close (depending on the parameter γ) to the matrix S_{reg}. For example, if the aim of the inverse problem is to find defects in an otherwise homogeneous medium, a suitable choice for S_{reg} could be a standard finite element stiffness matrix for a constant diffusion coefficient. In our practical computations, the regularization approach described in (3.8) generally led to better results.

We emphasize that the presented inversion process does not need to resolve any fine scales in order to obtain an effective numerical model. The information extracted by this procedure (i.e., the stiffness matrix $\tilde{S}_H$) may be used to simulate other problems subject to the same (unknown) diffusion coefficient. Furthermore, the information gathered can be seen as an intermediate step towards recovering information concerning the original coefficient itself. This additional recovery step will be studied in a future work.

4 Numerical Experiments

In this section, we present some numerical experiments that illustrate the capability of the proposed method. The inverse problem is based on synthetic data, i.e., the coarse measurements used to feed the inversion algorithm are obtained from finite element functions in V_h, defined on a mesh with mesh size $h = \sqrt{2} \cdot 2^{-9}$ that resolve the fine scale features of the diffusion coefficient. Furthermore, the data are perturbed by random noise with intensity up to 5%.

4.1 Example 1: full boundary data

In the first experiment, we assume to have full information on the operator (matrix) $\tilde{\mathfrak{L}}^{\text{eff}}$, i.e., we assume that measurements in Ω on the coarse scale $H = \sqrt{2} \cdot 2^{-5}$ for a complete basis of X_H are available. The scalar coefficient A for which the effective behavior should be recovered is constant on a mesh $\mathcal{T}_\varepsilon$ with $\varepsilon = \sqrt{2} \cdot 2^{-7}$ and the value on each element is independently obtained as a uniformly distributed random number between 1 and 50, i.e., for any $T \in \mathcal{T}_\varepsilon$ we have $A|_T \sim U(1, 50)$ (see Figure 4.1, left). We set $f = 1$ and start the inverse iteration with the finite element stiffness matrix S_H^0 based on the constant coefficient with value 1. The values of the functional $\mathcal{J}_H$ in the first 20 iterations of the

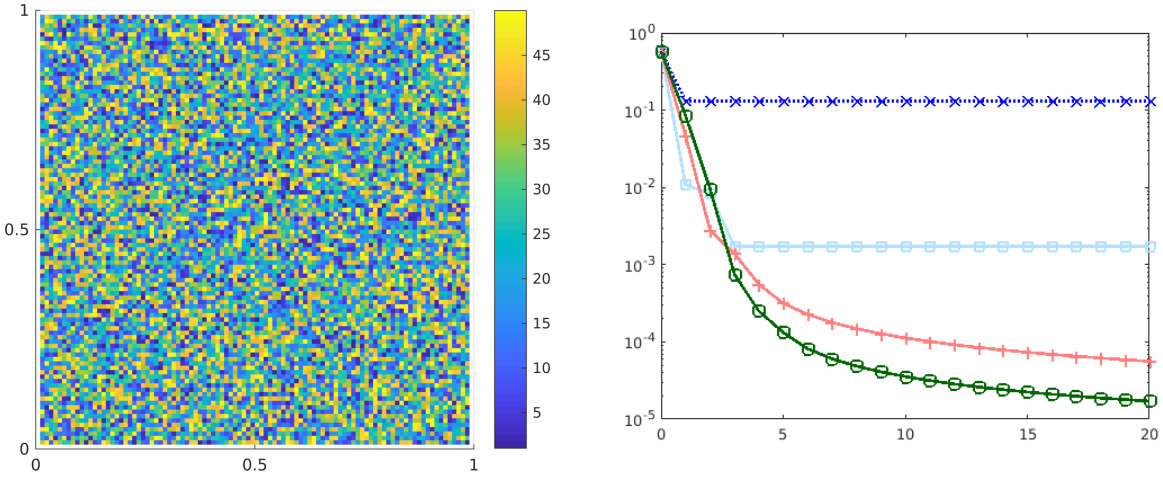

Figure 4.1: Left: Diffusion coefficient in Example 1. Right: Values of $\mathcal{J}_H$ in the first 20 iterations of the inversion algorithm, using sparsity patterns based on local matrices ((×, dotted) and quasi-local matrices with $\ell = 1$ (□), $\ell = 2$ (+) $\ell = 3$ (○).

inversion algorithm are given in Figure 4.1 (right). In particular, we compare the performance of a *local approach* based on matrices with the sparsity pattern of the standard finite element method (such as, e.g., the HMM or the Two-Scale Finite Element Method) with the proposed *quasi-local method* based on matrices in $\mathcal{M}(\ell, \mathcal{T}_H)$ for $\ell \in \{1, 2, 3\}$. One clearly sees that the quasi-local inversion leads to better results in terms of decrease and value of the error functional $\mathcal{J}_H$. In particular, with the local approach the functional seems to reach a stagnation relatively quickly, while the results significantly improve with the quasi-local approach when increasing the value of ℓ.

A necessary validation step, in order to further investigate the different methods, consists in solving a diffusion problem using the stiffness matrices reconstructed with the different approaches (local and quasi-local), and comparing the resulting numerical solutions with the finite element functions from which the measurements were taken to feed the inversion algorithm. The outcome of this assessment is shown in Figure 4.2, focusing on the cross sections at $x_2 = 0.5$ (left) and at $x_1 = 0.5$ (right) of

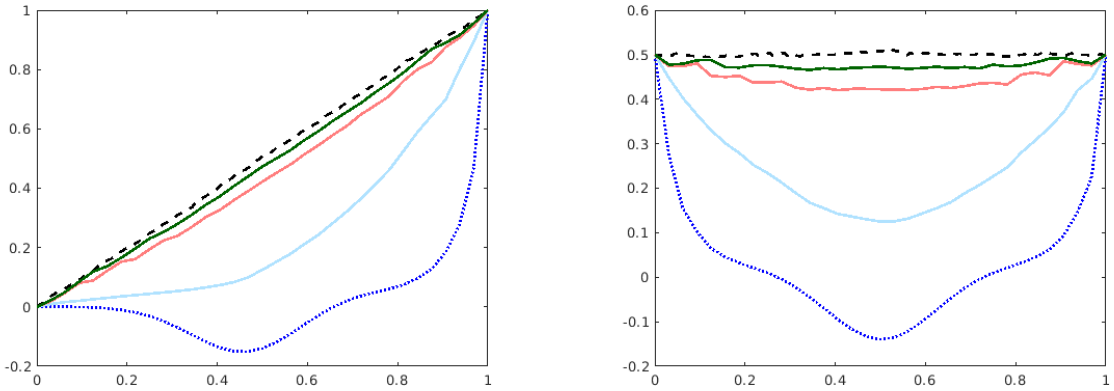

Figure 4.2: Cross sections of reconstructed functions with boundary condition $u^0(x_1, x_2) = x_1$ based on local stiffness matrices (●, dotted) and quasi-local ones with $\ell = 1$ (●), $\ell = 2$ (●), $\ell = 3$ (●) for Example 1 obtained from full boundary data. The corresponding fine FE function (●, dashed) is depicted as a reference. Left: Cross section at $x_2 = 0.5$. Right: Cross section at $x_1 = 0.5$.

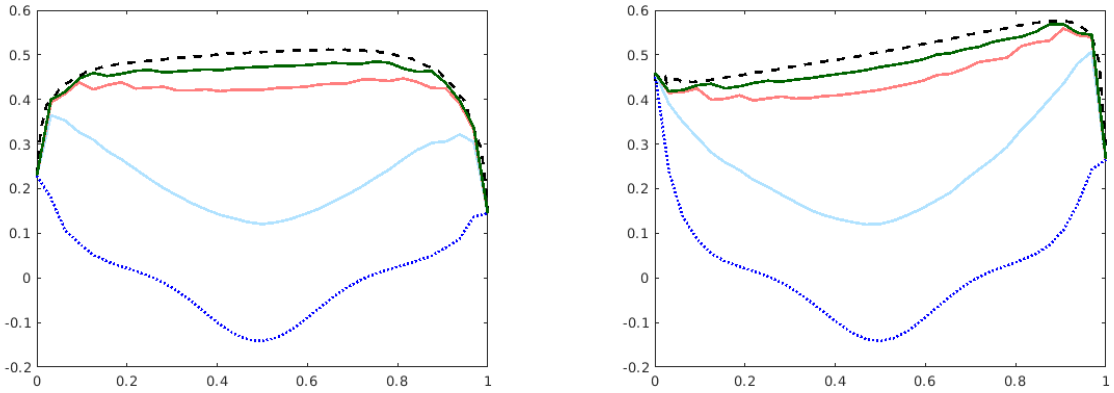

Figure 4.3: Cross sections of reconstructed functions with random boundary condition $u^0 \in X_H$ based on local stiffness matrices (●, dotted) and quasi-local ones with $\ell = 1$ (●), $\ell = 2$ (●), $\ell = 3$ (●) for Example 1 obtained from full boundary data. The corresponding fine FE function (●, dashed) is depicted as reference. Left: Cross section at $x_2 = 0.5$. Right: Cross section at $x_1 = 0.5$.

the numerical approximations corresponding to the boundary condition $u^0(x_1, x_2) = x_1$. Figure 4.3 depicts the same cross sections when a random boundary condition $u^0 \in X_H$ is considered.

Besides the accuracy of the numerical approximations computed based on the recovered stiffness matrices, it is also important to assess the robustness of the reconstructed effective model, i.e., to investigate to which extent the coarsened information about the diffusion coefficient encoded in the stiffness matrix can be used to simulate other scenarios.

For this purpose, we employ the reconstructed stiffness matrices to simulate a diffusion problem with two different right-hand sides, i.e.,

$$g_1(x_1, x_2) = 20\,(\mathbb{1}_{\{x_1<0.5\}}\,x_1 + \mathbb{1}_{\{x_1\geq 0.5\}}\,(1-x_1))(\mathbb{1}_{\{x_2<0.5\}}\,x_2 + \mathbb{1}_{\{x_2\geq 0.5\}}\,(1-x_2))$$

and

$$g_2(x_1, x_2) = 10\,\mathbb{1}_{\{x_1\geq 0.5\}},$$

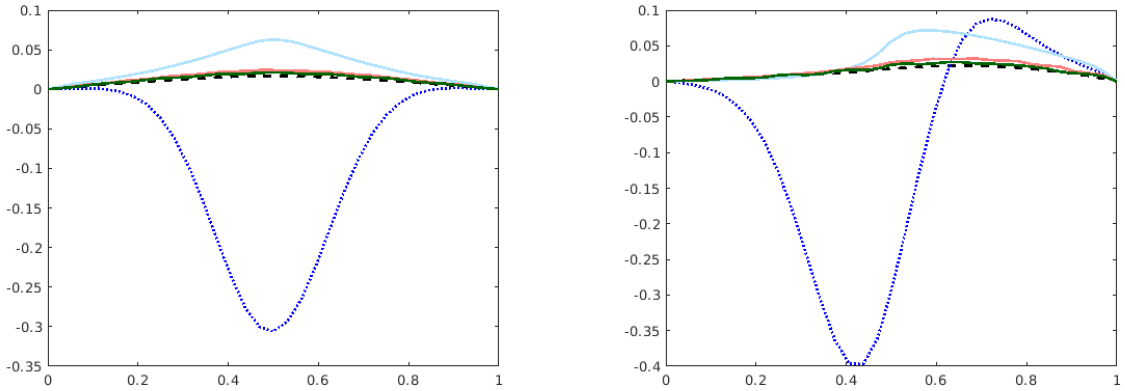

Figure 4.4: Cross sections at $x_2 = 0.5$ of reconstructed functions with homogeneous Dirichlet boundary conditions based on local stiffness matrices (●, dotted) and quasi-local ones with $\ell = 1$ (●), $\ell = 2$ (●), $\ell = 3$ (●). The corresponding fine FE functions (●, dashed) are given as a reference but were not part of the input data. Left: Right-hand side g_1. Right: Right-hand side g_2.

and compare the numerical results with the corresponding fine-scale solution using the diffusion coefficient depicted in Figure 4.1 (left). In both cases, homogeneous Dirichlet boundary conditions are imposed on the outer boundaries.

Representative cross sections of the numerical approximations obtained based on the reconstructed stiffness matrices, compared to the corresponding fine-scale solutions, are shown in Figure 4.4. The numerical results indicate that robustness can be assured only with the quasi-local inversion. Moreover, as in the previous experiments, the quality of the results improves if ℓ is increased.

4.2 Example 2: incomplete boundary data

Next, we consider a more realistic case where the operator $\tilde{\mathfrak{L}}^{\mathrm{eff}}$ is only partially known. In practice, this means that coarse measurements in Ω are available only for q distinct boundary conditions in X_H ($q < \dim X_H$). In this setting, the aim is to find an effective model that not only fits the given data, but that is also able to reproduce the coarse behavior for other boundary conditions not considered as input data.

The scalar coefficient A whose corresponding stiffness matrix should be recovered is shown in Figure 4.5 (left). We set $H = \sqrt{2} \cdot 2^{-5}$, $f = 1$, $q = 40$, and the initial matrix S_H^0 is defined as the finite element stiffness matrix based on an independent and identically distributed random coefficient on the coarse scale H with values between 0.1 and 10.

We adapt the *randomized approach* recently described in [34] in the context of deep learning. Namely, in each iteration step, we randomly choose half of the available data to compute the new search direction, whereas we use all available data for the line search and for the evaluation of the functional $\mathcal{J}_H$. The values of the error functional $\mathcal{J}_H$ in the first 20 iterations of the inversion algorithm are shown in Figure 4.5 (right). One can observe that classical local stiffness matrices and even the quasi-local approach with $\ell = 1$ cannot significantly improve the results obtained with the initial guess, while quasi-local matrices with $\ell \geq 2$ are able to reduce the values of the functional up to a certain degree.

As in the previous subsection, we validate the outcome of the inversion algorithm by solving a diffusion problem using the reconstructed stiffness matrices and comparing the numerical results with

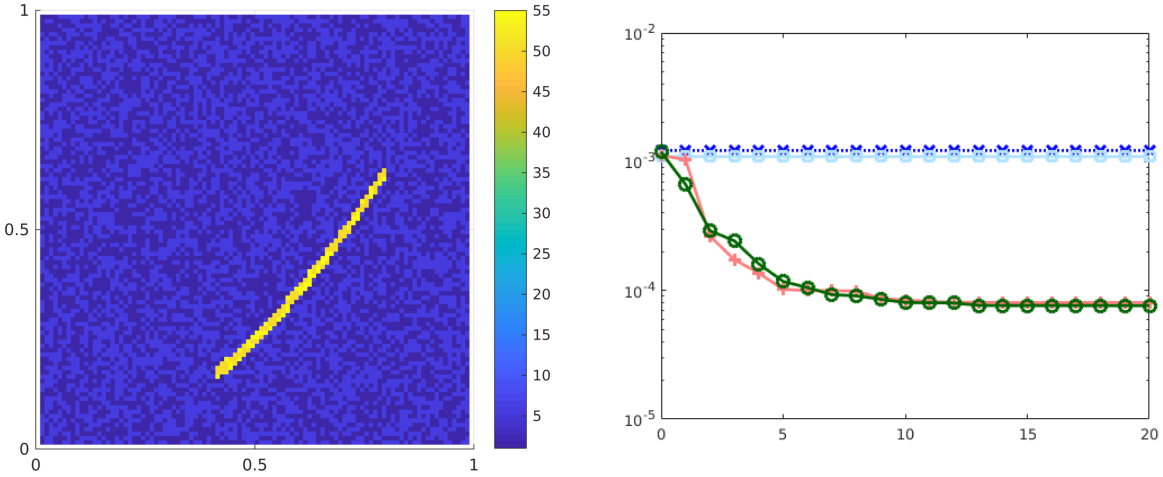

Figure 4.5: Left: Diffusion coefficient in Example 2. Right: Values of $\mathcal{J}_H$ in the first 20 iterations of the inversion algorithm based on local matrices ($\times$, dotted) and quasi-local matrices with $\ell = 1$ ($\square$), $\ell = 2$ ($+$) $\ell = 3$ ($\circ$).

the corresponding fine finite element solutions. The cross sections at $x_2 = 0.5$ and $x_1 = 0.5$ of the numerical approximations using the different stiffness matrices are shown in Figure 4.6, for the case with boundary condition $u^0(x_1, x_2) = x_1$. We emphasize that, in this setting, neither the reference finite element function (black dotted line in Figure 4.6) nor a coarse measurement from it were part of the input data.

For a further comparison, we also present in Figure 4.7 the same cross sections of the numerical solutions obtained from the stiffness matrices using a *full-data approach*, i.e., when all available data (40 measurements) are used in every step to compute the new search direction. The reconstructed matrices behave similarly to the ones obtained with the randomized approach, but we omit a detailed comparison of the two approaches. However, it is worth mentioning that the randomized strategy is generally more robust in the case of incomplete boundary data, and additionally requires less computational effort.

4.3 Discussion

The presented inversion results demonstrate that the reconstruction of the stiffness matrix assuming a sparsity pattern of classical finite elements does not allow to capture microscopic features of the problem, while the reconstruction based on a quasi-local approach, especially with $\ell \geq 2$, is able to mimic the effective behavior.

Furthermore, the quasi-local approach appears to be robust with respect to different right hand sides, a property which allows to employ the reconstructed effective model for the simulation of other scenarios, assuming that the microscopic properties remain unchanged.

Our experiments also indicate that a bound of the form $\ell \gtrsim |\log H|$ seems to be necessary and that ℓ needs to be increased for smaller values of H to obtain improvements in the first place. In that sense, our findings also deviate from the numerical results in [16] which indicate that truly local numerical homogenization might always be possible.

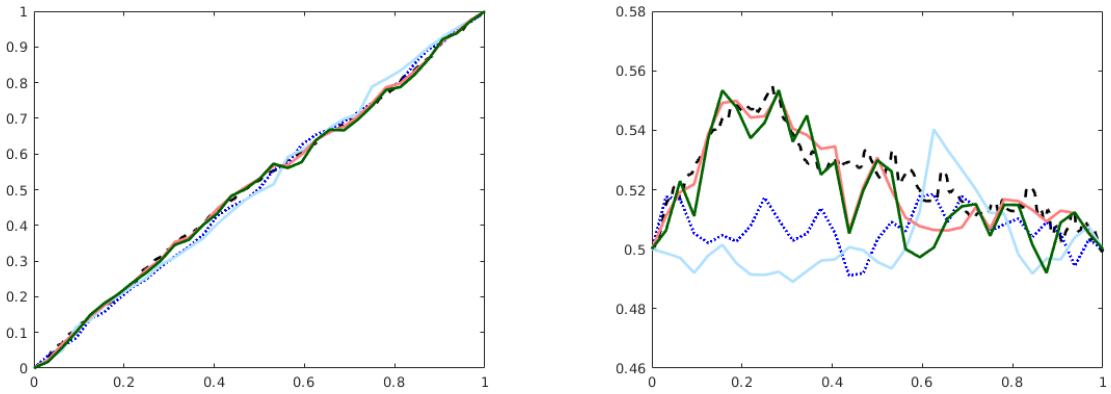

Figure 4.6: Cross sections of reconstructed functions with boundary condition $u^0(x_1, x_2) = x_1$ based on local stiffness matrices (●, dotted) and quasi-local ones with $\ell = 1$ (●), $\ell = 2$ (●), $\ell = 3$ (●) for Example 2 obtained from incomplete boundary data and the *randomized approach*. The corresponding fine FE function (●, dashed) is depicted as a reference but was not part of the input data. Left: Cross section at $x_2 = 0.5$. Right: Cross section at $x_1 = 0.5$.

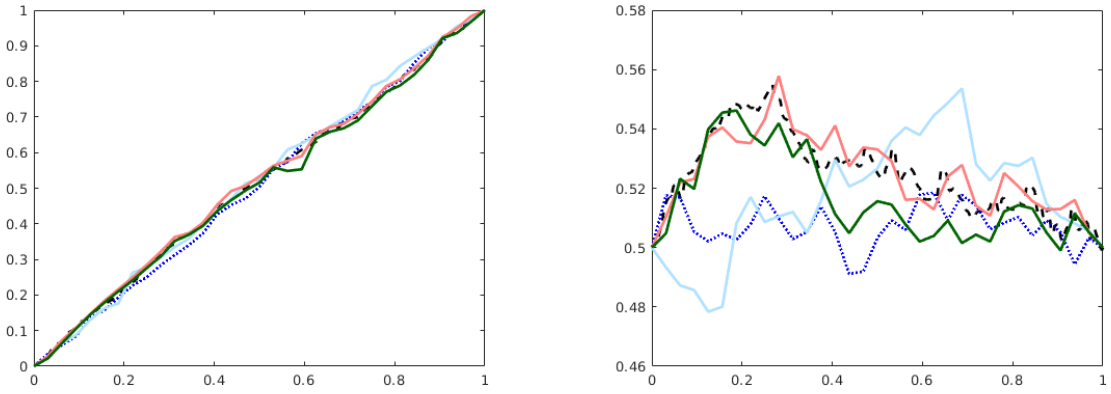

Figure 4.7: Cross sections of reconstructed functions with boundary condition $u^0(x_1, x_2) = x_1$ based on local stiffness matrices (●, dashed) and quasi-local ones with $\ell = 1$ (●), $\ell = 2$ (●), $\ell = 3$ (●) for Example 2 obtained from incomplete boundary data and the full-data approach. The corresponding fine FE function (●, dashed) is depicted as a reference but was not part of the input data. Left: Cross section at $x_2 = 0.5$. Right: Cross section at $x_1 = 0.5$.

5 Conclusion

We proposed a strategy to reconstruct the effective behavior of solutions of a multiscale diffusion model with a diffusion coefficient varying on a fine scale. The approach only uses information (measurements of the solutions) on a coarse scale level and is motivated by the effective models obtained by numerical homogenization. The method has a quasi-local nature in the sense that the reconstructed system matrices have a slightly denser sparsity pattern than standard finite element matrices, and this allows to recover characteristic fine scale features of the solutions without requiring numerical computations on the fine scale. The method has been numerically validated on a prototypical model problem, considering a stationary linear elliptic diffusion problem with inhomogeneous boundary conditions. In this setting, the numerical experiments indicate that the method is advantageous compared to approaches based on classical local models such as the finite element method or multiscale techniques such as the Heterogeneous Multiscale Method. Further, even the case of incomplete boundary data can be handled and ideas from learning-type methods may be adopted.

Future work will include the study of possible extensions in order to reconstruct, besides the behavior of the solution on the coarse scale, also the actual microscopic coefficients which defines the effective model on the discrete level. Additionally, we will also consider improvements of the method to even better handle the case of incomplete boundary data. For this purpose, more involved combinations with learning-type methods will be studied.

References

[1] Abdulle, A., Henning, P.: Localized orthogonal decomposition method for the wave equation with a continuum of scales. Math. Comp. **86**(304), 549–587 (2017)

[2] Altmann, R., Chung, E., Maier, R., Peterseim, D., Pun, S.M.: Computational multiscale methods for linear heterogeneous poroelasticity. ArXiv e-prints **1801.00615** (2018)

[3] Babuska, I., Lipton, R.: Optimal local approximation spaces for generalized finite element methods with application to multiscale problems. Multiscale Model. Simul. **9**(1), 373–406 (2011). DOI 10.1137/100791051. URL http://dx.doi.org/10.1137/100791051

[4] Babuska, I.M., Sauter, S.A.: Is the pollution effect of the FEM avoidable for the Helmholtz equation considering high wave numbers? SIAM J. Numer. Anal. **34**(6), 2392–2423 (1997)

[5] Calderón, A.P.: On an inverse boundary. In: Seminar on Numerical Analysis and its Applications to Continuum Physics, Rio de Janeiro, 1980, pp. 65–73. Brazilian Math. Soc. (1980)

[6] Chung, E.T., Efendiev, Y., Leung, W.T.: Constraint energy minimizing generalized multiscale finite element method. Comput. Methods Appl. Mech. Engrg. **339**, 298–319 (2018)

[7] Cottrell, J.A., Hughes, T.J.R., Bazilevs, Y.: Isogeometric analysis: toward integration of CAD and FEA. John Wiley & Sons (2009)

[8] Du, Q.: Nonlocal calculus of variations and well-posedness of peridynamics. In: Handbook of Peridynamic Modeling, pp. 101–124. Chapman and Hall/CRC (2016)

[9] E, W., Engquist, B.: The heterogeneous multi-scale method for homogenization problems. In: Multiscale methods in science and engineering, *Lect. Notes Comput. Sci. Eng.*, vol. 44, pp. 89–110. Springer (2005)

[10] E, W., Engquist, B., et al.: The heterogeneous multiscale methods. Commun. Math. Sci. **1**(1), 87–132 (2003)

[11] Efendiev, Y., Galvis, J., Hou, T.Y.: Generalized multiscale finite element methods (GMsFEM). J. Comput. Phys. **251**, 116–135 (2013)

[12] Ern, A., Guermond, J.L.: Finite element quasi-interpolation and best approximation. ESAIM: M2AN **51**(4), 1367–1385 (2017)

[13] Gallistl, D., Henning, P., Verfürth, B.: Numerical homogenization of H(curl)-problems. SIAM J. Numer. Anal. **56**, 1570–1596 (2018)

[14] Gallistl, D., Peterseim, D.: Stable multiscale Petrov–Galerkin finite element method for high frequency acoustic scattering. Comput. Methods Appl. Mech. Engrg. **295**, 1–17 (2015)

[15] Gallistl, D., Peterseim, D.: Computation of quasi-local effective diffusion tensors and connections to the mathematical theory of homogenization. Multiscale Model. Simul. **15**(4), 1530–1552 (2017)

[16] Grasedyck, L., Greff, I., Sauter, S.: The AL basis for the solution of elliptic problems in heterogeneous media. Multiscale Model. Simul. **10**(1), 245–258 (2012)

[17] Hellman, F., Målqvist, A.: Contrast independent localization of multiscale problems. Multiscale Model. Simul. **15**(4), 1325–1355 (2017)

[18] Henning, P., Målqvist, A., Peterseim, D.: A localized orthogonal decomposition method for semilinear elliptic problems. ESAIM: M2AN **48**(05), 1331–1349 (2014)

[19] Henning, P., Persson, A.: A multiscale method for linear elasticity reducing Poisson locking. Comput. Methods Appl. Mech. Engrg. **310**, 156–171 (2016)

[20] Henning, P., Peterseim, D.: Oversampling for the multiscale finite element method. Multiscale Model. Simul. **11**(4), 1149–1175 (2013)

[21] Hirsch, S., Sack, I., Braun, J.: Magnetic resonance elastography: physical background and medical applications. John Wiley & Sons (2017)

[22] Hou, T.Y., Wu, X.H.: A multiscale finite element method for elliptic problems in composite materials and porous media. J. Comput. Phys. **134**(1), 169–189 (1997). DOI 10.1006/jcph.1997.5682. URL http://dx.doi.org/10.1006/jcph.1997.5682

[23] Hughes, T.J.R., Cottrell, J.A., Bazilevs, Y.: Isogeometric analysis: CAD, finite elements, NURBS, exact geometry and mesh refinement. Comput. Methods Appl. Mech. Engrg. **194**(39-41), 4135–4195 (2005)

[24] Kornhuber, R., Peterseim, D., Yserentant, H.: An analysis of a class of variational multiscale methods based on subspace decomposition. Math. Comp. **published electronically** (2018). DOI 10.1090/mcom/3302

[25] Lipton, R.: Dynamic brittle fracture as a small horizon limit of peridynamics. J. Elasticity **117**(1), 21–50 (2014)

[26] Maier, R., Peterseim, D.: Explicit computational wave propagation in micro-heterogeneous media. BIT Numer. Math. (2018). Online first

[27] Målqvist, A., Peterseim, D.: Localization of elliptic multiscale problems. Math. Comp. **83**(290), 2583–2603 (2014)

[28] Matache, A.M., Schwab, C.: Two-scale FEM for homogenization problems. ESAIM: M2AN **36**(4), 537–572 (2002)

[29] Melenk, J.M., Parsania, A., Sauter, S.: General DG-methods for highly indefinite Helmholtz problems. J. Sci. Comput. **57**(3), 536–581 (2013)

[30] Melenk, J.M., Sauter, S.: Convergence analysis for finite element discretizations of the Helmholtz equation with Dirichlet-to-Neumann boundary conditions. Math. Comp. **79**(272), 1871–1914 (2010)

[31] Melenk, J.M., Sauter, S.: Wavenumber explicit convergence analysis for Galerkin discretizations of the Helmholtz equation. SIAM J. Numer. Anal. **49**(3), 1210–1243 (2011)

[32] Muthupillai, R., Ehman, R.L.: Magnetic resonance elastography. Nat. Med. **2**, 601–603 (1996)

[33] Owhadi, H.: Multigrid with rough coefficients and multiresolution operator decomposition from hierarchical information games. SIREV **59**(1), 99–149 (2017). DOI 10.1137/15M1013894. URL http://dx.doi.org/10.1137/15M1013894

[34] Owhadi, H., Yoo, G.R.: Kernel flows: from learning kernels from data into the abyss. ArXiv e-prints **1808.04475** (2018)

[35] Owhadi, H., Zhang, L., Berlyand, L.: Polyharmonic homogenization, rough polyharmonic splines and sparse super-localization. ESAIM: M2AN **48**(2), 517–552 (2013)

[36] Peterseim, D.: Variational multiscale stabilization and the exponential decay of fine-scale correctors. In: Building Bridges: Connections and Challenges in Modern Approaches to Numerical Partial Differential Equations, pp. 341–367. Springer (2016)

[37] Peterseim, D.: Eliminating the pollution effect in Helmholtz problems by local subscale correction. Math. Comp. **86**(305), 1005–1036 (2017)

[38] Peterseim, D., Scheichl, R.: Robust numerical upscaling of elliptic multiscale problems at high contrast. Comput. Methods Appl. Math. **16**, 579–603 (2016). DOI 10.1515/cmam-2016-0022

[39] Sack, I., Beierbach, B., Hamhaber, U., Klatt, D., Braun, J.: Non-invasive measurement of brain viscoelasticity using magnetic resonance elastography. NMR Biomed. **21**(3), 265–271 (2008)

[40] Silling, S.A.: Reformulation of elasticity theory for discontinuities and long-range forces. J. Mech. Phys. Solids **48**(1), 175–209 (2000)

[41] Verfürth, B.: Numerical homogenization for indefinite H(curl)-problems. In: K. Mikula, D. Sevcovic, J. Urban (eds.) Proceedings of Equadiff 2017 conference, pp. 137–146. Slovak University of Technology, Bratislava (2017)